Meas. Sci. Technol. **8** (1997) 1379–1392. Printed in the UK PII: S0957-0233(97)84477-3

Fundamentals of digital particle image velocimetry

J Westerweel

Laboratory for Aero & Hydrodynamics, Delft University of Technology, Rotterdamseweg 145, 2628 AL Delft, The Netherlands

Received 28 May 1997, accepted for publication 27 August 1997

Abstract. The measurement principle of digital particle image velocimetry (PIV) is described in terms of linear system theory. The conditions for PIV correlation analysis as a valid interrogation method are determined. Limitations of the method arise as consequences of the implementation. The theory is applied to investigate the statistical properties of the analysis and to optimize and improve the measurement performance. The theoretical results comply with results from Monte Carlo simulations and test measurements described in the literature. Examples of both correct and incorrect implementations are given.

1. Introduction

Optical flow diagnostics are based on the interaction, i.e. refraction, absorption or scattering, of (visible) light with inhomogeneous media. In an optically homogeneous fluid there is no significant interaction of the incident light with the fluid, such as refraction, by which information of the flow velocity field can be retrieved. In particle image velocimetry (PIV) the fluid motion is made visible by adding small tracer particles and from the positions of these tracer particles at two instances of time, i.e. the particle displacement, it is possible to infer the flow velocity field.

The initial groundwork for a PIV theory was laid down by Adrian (1988) who described the expectation value of the auto-correlation function for a double-exposure continuous PIV image. This description provided the framework for experimental design rules (Keane and Adrian 1990). Later, the theory was generalized to include multiple-exposure recordings (Keane and Adrian 1991) and cross-correlation analysis (Keane and Adrian 1993). The theory provided an adequate description for the analysis of highly resolved PIV photographs, which was the common mode of operation for a considerable time. However, nowadays PIV has developed towards the use of electronic cameras for direct recording of the particle images (Willert and Gharib 1991). As the resolution and image format of electronic cameras is several orders of magnitude lower than that of a photographic medium, digitization cannot be ignored. The theory was further extended by Westerweel (1993a) to include digital PIV images and the estimation of the displacement at sub-pixel level.

This paper summarizes the fundamental aspects of PIV signal analysis. The measurement principle is described in terms of (linear) system theory, in which the tracer particles are viewed as an observable pattern that is tied to the fluid; the observed tracer patterns at two subsequent instances are considered as the input and output of the system, and the velocity field is inferred from the analysis of the input and output signals. The tracer pattern is then related to the observed (digital) image. The statistical description of discrete PIV images is subsequently applied to evaluate the estimation of the particle-image displacement as a function of the spatial resolution.

The development of the theory is based on descriptions of random processes and random fields given by e.g. Priestley (1992) and Rosenfeld and Kak (1982). This work only presents the main results; for detailed derivations the reader is also advised to consult Westerweel (1993a). A summary of the statistical properties of sub-pixel interpolation for images with low pixel resolution is also available as a conference paper (Westerweel 1993b).

2. Acquisition

2.1. The displacement field

In PIV the fluid velocity is inferred from the motion of tracer particles. The tracer particles are considered as *ideal* when they (1) exactly follow the motion of the fluid, (2) do not alter the flow or the fluid properties and (3) do not interact with each other. The velocity is measured indirectly, as a displacement $\boldsymbol{D}(\boldsymbol{X};t',t'')$ of the tracer particles in a finite time interval $\Delta t = t'' - t'$, i.e.

$$\boldsymbol{D}(\boldsymbol{X};t',t'') = \int_{t'}^{t''} \boldsymbol{v}[\boldsymbol{X}(t),t]\,\mathrm{d}t \qquad (1)$$

where $\boldsymbol{v}[\boldsymbol{X}(t)]$ is the velocity of the tracer particle. For ideal tracer particles the tracer velocity $\boldsymbol{v}$ is equal to the local fluid velocity $\boldsymbol{u}(\boldsymbol{X},t)$. However, in a practical situation the concept of ideal tracers can only be approximated. In addition, equation (1) implies that the displacement field only provides information about the

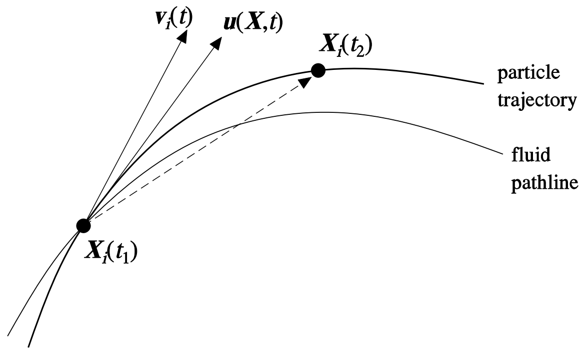

Figure 1. The displacement of the tracer particles is an approximation of the fluid velocity (after Adrian 1995).

average velocity along the trajectory over a time Δt. This is illustrated in figure 1.

Thus, $\boldsymbol{D}$ cannot lead to an exact representation of $\boldsymbol{u}$, but approximates it within a finite error ε:

$$\|\boldsymbol{D} - \boldsymbol{u} \cdot \Delta t\| < \varepsilon. \tag{2}$$

The associated error is often negligible, provided that the spatial and temporal scales of the flow are large with respect to the spatial resolution and the exposure time delay, and the dynamics of the tracer particles. A further analysis of these aspects is given by Adrian (1995).

The flow information is only obtained from the locations at which the tracer particles are present. Since these are distributed randomly over the flow, the displacement of individual tracer particles constitutes a random sampling of the displacement field, and different realizations yield different estimates of $\boldsymbol{D}$. Obviously, these differences can be neglected as long as the reconstructed displacement field satisfies equation (2). This implies that the displacement field should be sampled at a density that matches the smallest length scale of the spatial variations in $\boldsymbol{D}$. Since $\boldsymbol{D}$ can be regarded as a low-pass filtered representation of $\boldsymbol{u}$, with a cut-off filter length that is equal to $\|\boldsymbol{D}\|$, the displacement field should be sampled with an average distance that is *smaller* than the particle displacement. This implies that a measurement in which the average distance between distinct particle images is *larger* than the displacement (as is the case in conventional particle tracking; see figure 2(a)) cannot resolve the full displacement field. However, when the seeding concentration is high (so that the mean spacing between tracer particles is smaller than the displacement) it is not possible to identify matching particle pairs unambiguously; see figure 2(b). It is therefore more convenient to describe the tracer particles in terms of a *pattern*.

2.2. The tracer pattern

The tracer particles constitute a random pattern that is 'tied' to the fluid and the fluid motion is visible through changes of the tracer pattern. The tracer pattern in $\boldsymbol{X}$ at time t is defined as:

$$G(\boldsymbol{X}, t) = \sum_{i=1}^{\mathcal{N}} \delta[\boldsymbol{X} - \boldsymbol{X}_i(t)] \tag{3}$$

where $\mathcal{N}$ is the total number of particles in the flow, $\delta(\boldsymbol{X})$ is the Dirac δ-function and $\boldsymbol{X}_i(t)$ the position vector of the particle with index i at time t. Integration of $G(\boldsymbol{X}, t)$ over a volume yields the number of particles in that volume.

The tracer pattern at time t' can be viewed as a spatial signal $G'(\boldsymbol{X}) = G(\boldsymbol{X}, t')$ at the input of a 'black-box' system (representing the flow) that acts on the input signal, and returns a new signal $G''(\boldsymbol{X}) = G(\boldsymbol{X}, t'')$ at the output; see figure 3. For ideal tracer particles the addition of a new particle does not affect the action of the system on the other tracer particles, i.e. the system is linear. Consequently, the output signal can be written as a convolution of the input signal with the impulse response H of the system:

$$G''(\boldsymbol{X}) = \int H(\boldsymbol{X}, \boldsymbol{X}') G'(\boldsymbol{X}') \, \mathrm{d}\boldsymbol{X}'. \tag{4}$$

The impulse response is a shift of the input by the local displacement $\boldsymbol{D}$ in equation (1):

$$H(\boldsymbol{X}', \boldsymbol{X}'') = \delta[\boldsymbol{X}'' - \boldsymbol{X}' - \boldsymbol{D}]. \tag{5}$$

The shift formally depends on $\boldsymbol{X}$, but under equation (2) it can be assumed that $\boldsymbol{D}$ is locally uniform, so that H can be regarded as shift invariant, i.e. $H(\boldsymbol{X}', \boldsymbol{X}'') = H(\boldsymbol{X}'' - \boldsymbol{X}')$.

According to linear system theory, the impulse response of a black-box system can be obtained from the cross-covariance $R_{G'G''}$ of a random input signal with the corresponding output signal:

$$R_{G'G''}(\boldsymbol{s}) = H * R_{G'}(\boldsymbol{s}) \tag{6}$$

(Priestley 1992), where $*$ denotes a convolution integral, and $R_{G'}$ is the auto-covariance of the input signal. For the special case where the input signal is a homogeneous white process (i.e. $R_{G'}(\boldsymbol{s}) \propto \delta(\boldsymbol{s})$), the cross-correlation directly yields the impulse response.

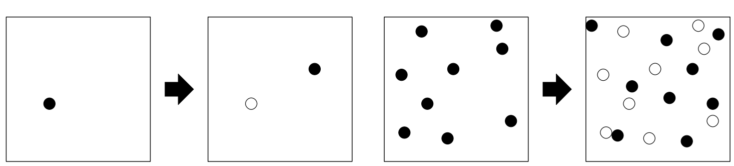

Figure 2. (a) At low seeding density individual tracers yield the fluid motion; (b) at high seeding density the tracers constitute a pattern that is advected by the flow.

$$G(\vec{X},t') \longrightarrow \boxed{\vec{v}(\vec{X},t)} \longrightarrow G(\vec{X},t'')$$

Figure 3. The velocity field $\boldsymbol{v}(\boldsymbol{X}, t)$ is viewed as a black-box system that acts on the tracer pattern $G(\boldsymbol{X}, t')$ at the input to yield the tracer pattern $G(\boldsymbol{X}, t'')$ at the output.

2.3. The tracer ensemble

Following Adrian (1988), the statistical properties of the tracers are evaluated by considering the ensemble of all possible realizations of $G(\boldsymbol{X}, t)$ for a given (fixed) flow field $\boldsymbol{u}(\boldsymbol{X}, t)$. The ensemble cross-covariance is defined as:

$$R_{G'G''}(\boldsymbol{X}', \boldsymbol{X}'') = \langle G'(\boldsymbol{X}')G''(\boldsymbol{X}'')\rangle - \langle G'(\boldsymbol{X}')\rangle\langle G''(\boldsymbol{X}'')\rangle \tag{7}$$

where $\langle\cdots\rangle$ denotes the ensemble average.

To evaluate the terms in (7), the tracer pattern defined in (3) is represented as a single vector in a $3\mathcal{N}$-dimensional phase space:

$$\boldsymbol{\Gamma}(t) = \begin{pmatrix} \boldsymbol{X}_1(t) \\ \boldsymbol{X}_2(t) \\ \vdots \\ \boldsymbol{X}_{\mathcal{N}}(t) \end{pmatrix}. \tag{8}$$

For *ideal* tracer particles the trajectory of $\boldsymbol{\Gamma}$ is prescribed by the velocity field at the positions of the tracer particles:

$$\frac{\mathrm{d}\boldsymbol{\Gamma}}{\mathrm{d}t} = \boldsymbol{\mathcal{U}}(\boldsymbol{\Gamma}, t) \qquad \text{with } \boldsymbol{\mathcal{U}}(\boldsymbol{\Gamma}, t) = \begin{pmatrix} \boldsymbol{u}(\boldsymbol{X}_1, t) \\ \boldsymbol{u}(\boldsymbol{X}_2, t) \\ \vdots \\ \boldsymbol{u}(\boldsymbol{X}_{\mathcal{N}}, t) \end{pmatrix}. \tag{9}$$

The ensemble mean of $G(\boldsymbol{X})$ is given by:

$$\langle G\rangle = \int G(\boldsymbol{\Gamma})\varrho(\boldsymbol{\Gamma})\,\mathrm{d}\boldsymbol{\Gamma} \tag{10}$$

(for brevity of notation the coordinates $\boldsymbol{X}$ and t are omitted) where $\varrho(\boldsymbol{\Gamma})$ is the probability density function (PDF) for $\boldsymbol{\Gamma}$. The second-order statistic $\langle G'G''\rangle$ is given by:

$$\langle G'G''\rangle = \iint G(\boldsymbol{\Gamma}')G(\boldsymbol{\Gamma}'')\varrho(\boldsymbol{\Gamma}''|\boldsymbol{\Gamma}')\varrho(\boldsymbol{\Gamma})\,\mathrm{d}\boldsymbol{\Gamma}'\,\mathrm{d}\boldsymbol{\Gamma}'' \tag{11}$$

where $\varrho(\boldsymbol{\Gamma}''|\boldsymbol{\Gamma}')$ is the conditional PDF for $\boldsymbol{\Gamma}''$ given the initial state $\boldsymbol{\Gamma}'$. For a given flow field $\boldsymbol{\Gamma}''$ is uniquely determined by (9), and therefore

$$\varrho(\boldsymbol{\Gamma}''|\boldsymbol{\Gamma}') = \delta[\boldsymbol{\Gamma}'' - \boldsymbol{\Gamma}' - \boldsymbol{\mathcal{D}}] \qquad \text{with } \boldsymbol{\mathcal{D}} = \int_{t'}^{t''} \boldsymbol{\mathcal{U}}[\boldsymbol{\Gamma}(t)]\,\mathrm{d}t \tag{12}$$

(cf equation (1)). As a direct consequence (11) reduces to:

$$\langle G'G''\rangle = \int G(\boldsymbol{\Gamma})G(\boldsymbol{\Gamma} + \boldsymbol{\mathcal{D}})\varrho(\boldsymbol{\Gamma})\,\mathrm{d}\boldsymbol{\Gamma}. \tag{13}$$

Thus, both first- and second-order ensemble statistics are determined by $\varrho(\boldsymbol{\Gamma})$ (for ideal tracer particles).

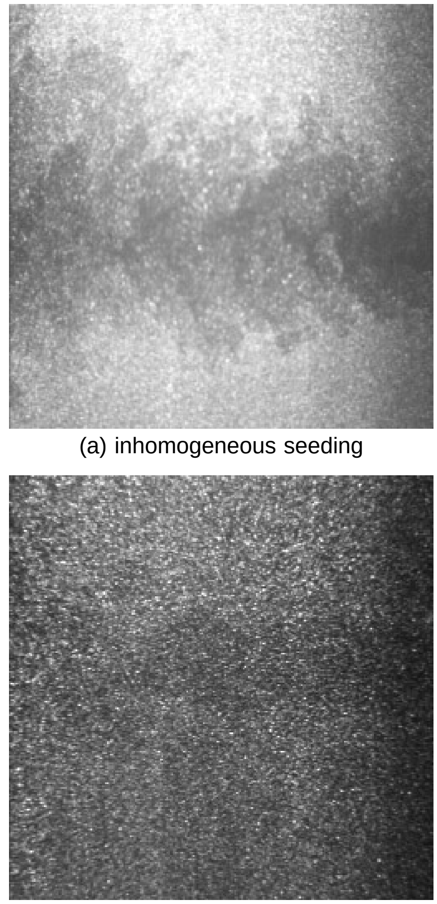

(a) inhomogeneous seeding

(b) homogeneous seeding

Figure 4. Seeding of a jet flow for (a) flow visualization and (b) PIV.

Since there are no particles that appear into or disappear from the ensemble, ϱ satisfies a continuity equation:

$$\frac{\partial\varrho}{\partial t} + \boldsymbol{\mathcal{U}}\cdot\operatorname{grad}\varrho + \varrho\operatorname{div}\boldsymbol{\mathcal{U}} = 0 \tag{14}$$

(this is essentially a formulation of Liouville's theorem). Consider the special case of an incompressible flow with spatially homogeneous seeding, i.e.

$$\operatorname{grad}\varrho = \boldsymbol{0} \qquad \text{and } \operatorname{div}\boldsymbol{\mathcal{U}} = 0. \tag{15}$$

Inserting this into (14) immediately yields:

$$\frac{\partial\varrho}{\partial t} = 0 \tag{16}$$

which implies that $\varrho(,t)$ is constant and does not depend on the flow field. Hence, a homogeneous tracer pattern can only be maintained for ideal tracer particles in an incompressible flow field.

In the limit for $V \to \infty$ and $\mathcal{N} \to \infty$, with $\mathcal{N}/V = C$ is constant, where C is the number density of the seeding, the first- and second-order statistics are given by

$$\begin{cases} \langle G'(\boldsymbol{X})\rangle = \langle G''(\boldsymbol{X})\rangle = C \\ \langle G'(\boldsymbol{X}')G''(\boldsymbol{X}'')\rangle = C\delta[\boldsymbol{X}'' - \boldsymbol{X}' - \boldsymbol{D}] + C^2 \end{cases} \tag{17}$$

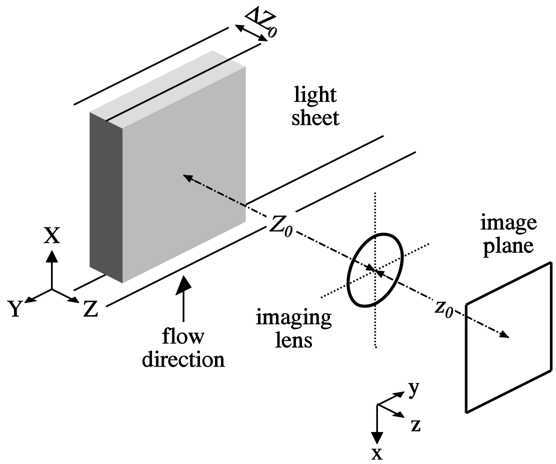

Figure 5. Schematic representation of the imaging set-up in PIV.

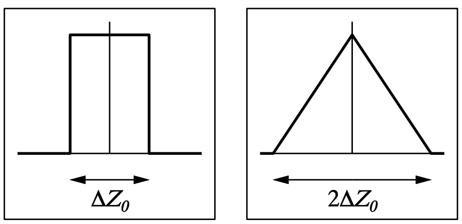

(a) $I_0(Z)$ (b) $F_O(w\Delta t)$

Figure 6. The loss-of-correlation F_O due to out-of-plane motion ($w\Delta t$) for a light sheet $I_o(Z)$ with a uniform intensity profile.

(Westerweel 1993a). So, (7) yields:

$$R_{G'G''}(\boldsymbol{X}', \boldsymbol{X}'') = C\delta[\boldsymbol{X}'' - \boldsymbol{X}' - \boldsymbol{D}]. \tag{18}$$

This implies that an interpretation of the cross-covariance in terms of the tracer displacement is only appropriate for an incompressible flow with a homogeneous seeding of ideal tracers. In other cases the location of the correlation peak is not purely determined by the flow field, but is biased with respect to the distribution of the seeding over the flow. For those cases where the correlation analysis is not appropriate, the analysis could be made using a different method, for example by a particle tracking algorithm (Keane *et al* 1995).

This analysis also demonstrates the difference between seeding for flow *visualization* and for PIV. For flow visualization, the aim is to make certain flow structures or flow regions visible. This can be accomplished by introducing the seeding at a particular location (i.e. inhomogeneous seeding). By contrast, a single-exposure PIV recording of an incompressible flow with (ideal) homogeneous seeding appears featureless; any flow structure only becomes visible when the velocity field is evaluated.

This is illustrated in figure 4, which shows two (single-exposure) images of the same jet flow. In one case only the ambient fluid was seeded, which clearly visualizes the jet, but which is unsuitable for PIV measurement. If both the jet and the ambient fluid are seeded correctly it is no longer possible to distinguish between the ambient fluid and the jet fluid.

2.4. Imaging

In planar domain PIV, a cross section of the flow is illuminated with a thin light sheet, and the tracer particles in the light sheet are projected onto a recording medium in the image plane of a lens, as illustrated in figure 5. The intensity of the light sheet thickness ΔZ_0 is assumed to change only in the Z-direction It is assumed that the optics consist of an aberration-free circular lens with a numerical aperture $f^{\#}$, and that all observed particles are in focus (which is satisfied when ΔZ_0 is less than the object focal depth (Adrian 1991)).

The imaging of the tracer pattern is essentially a projection of the tracer pattern onto the planar domain, i.e.

$$g(x, y) = \frac{1}{I_Z} \int I_o(Z) G(X, Y, Z)\, \mathrm{d}Z \tag{19}$$

with $x = MX$ and $y = MY$, where $I_o(Z)$ is the light-sheet intensity profile with a maximum I_Z and M is the image magnification. A paraxial approximation is assumed, so that the projection of G onto g only involves an integration along the Z-coordinate. By analogy with $G(X, Y, Z)$, the integral of $g(x, y)$ over a given area yields the (non-integer) number of particle images in that area. The ensemble cross-covariance of g' and g'' is given by:

$$R_{g'g''}(\boldsymbol{s}) = F_O(\Delta Z) \cdot C\Delta Z_0 \cdot \delta(\boldsymbol{s} - \boldsymbol{s}_D) \tag{20}$$

(cf (18)), with

$$F_O(\Delta Z) = \int I_o(Z) I_o(Z + \Delta Z)\, \mathrm{d}Z \Big/ \int I_o^2(Z)\, \mathrm{d}Z \tag{21}$$

(Adrian 1988), and where $\boldsymbol{s}_D = M \cdot (\Delta X, \Delta Y)$ is the in-plane displacement of the tracer images. The term F_O represents the *loss of correlation* due to tracer particles that enter or leave the light sheet.

For a uniform light sheet, F_O is proportional to the magnitude of the out-of-plane displacement; see figure 6. This information can be used to determine the magnitude of the out-of-plane displacement (Raffel *et al* 1996).

The image of a single tracer particle is denoted by $t(x, y)$, which has a finite width d_t (i.e. particle-image diameter). The appearance of the image depends on the concentration of tracer particles in the light sheet. The source density is defined as:

$$N_S = C\Delta Z_0 M^{-2} \frac{\pi}{4} d_t^2 \tag{22}$$

(Adrian 1984). At a low source density ($N_S \ll 1$) the average distance between particles is much larger than the particle-image diameter, and the image consists of *isolated* particle images; at a high source density ($N_S \gg 1$) particle images overlap, and for coherent illumination the resultant image is a random interference pattern, better known as speckle.

The optical system described in figure 5 can be considered as a linear, shift-invariant system, with $t(x, y)$

the system response to a single tracer particle. Then, for identical tracer particles, the image intensity $I(x, y)$ at low source density is given by:

$$I(x, y) = I_Z \iint t(s - x, t - y) g(s, t)\, \mathrm{d}s\, \mathrm{d}t. \tag{23}$$

The corresponding image ensemble cross-covariance is given by:

$$R_{II}(\boldsymbol{s}) = F_O(\Delta Z) \cdot R_I * \delta(\boldsymbol{s} - \boldsymbol{s}_D) \tag{24}$$

(cf equation (6)), where $R_I(\boldsymbol{s})$ is the image auto-correlation:

$$R_I(\boldsymbol{s}) = C \Delta Z_0 M^{-2} I_Z^2 t_0^2 F_t(\boldsymbol{s}) \tag{25}$$

F_t is the particle-image self-correlation and t_0^2 a normalization term ($t_0^2 F_t = t * t$). For small particle images, R_{II} has the shape of a narrow peak with a width that is proportional to d_t. The location of this peak is determined by the in-plane particle-image displacement, and the peak amplitude is proportional to the number of tracer particles per unit area that remain within the light sheet (i.e. $F_O C \Delta Z_0 M^{-2}$). In the next section this model for the image ensemble statistics is applied to describe the statistical properties of the interrogation of PIV images.

3. Interrogation

3.1. Spatial correlation

So far, an ensemble of all possible realizations of the tracer pattern has been considered. In practice the flow field is not reproducible (e.g. turbulent flow) and only a single realization of I' and I'' is available. In that case ensemble averaging is replaced by spatial averaging, defined as

$$C(\boldsymbol{s}) = \iint W'(\boldsymbol{x}) I'(\boldsymbol{x}) W''(\boldsymbol{x} + \boldsymbol{s}) I''(\boldsymbol{x} + \boldsymbol{s})\, \mathrm{d}\boldsymbol{x} \tag{26}$$

(Adrian 1988) where W' and W'' are window functions that are associated with the interrogation domains in I' and I'' respectively.

A necessary condition is that the spatial averaging is ergodic with respect to the ensemble averaging, which implies that the spatial average over an interrogation domain converges to the ensemble average when the domain area goes to infinity (Rosenfeld and Kak 1982, Priestley 1992). This condition is satisfied when the tracer pattern is homogeneous and the impulse response is shift invariant. Hence, the spatial correlation can be written as the sum of an ensemble mean value $\langle C(\boldsymbol{s}) \rangle$ and a fluctuation $C'(\boldsymbol{s})$ with respect to the mean:

$$C(\boldsymbol{s}) = \langle C(\boldsymbol{s}) \rangle + C'(\boldsymbol{s}) = R_D(\boldsymbol{s}) + R_C(\boldsymbol{s}) + R_F(\boldsymbol{s}) + C'(\boldsymbol{s}) \tag{27}$$

(Adrian 1988) where $R_D(\boldsymbol{s})$ is the so-called *displacement-correlation* peak, R_C is a constant background correlation term and R_F represents the correlation between the mean and fluctuating image intensities. The displacement-correlation peak is given by:

$$R_D(\boldsymbol{s}) = N_I F_I F_O \cdot I_Z^2 t_0^2 F_t * \delta(\boldsymbol{s} - \boldsymbol{s}_D) \tag{28}$$

with the image density N_I given by

$$N_I = C \Delta Z_0 D_I^2 / M^2 \tag{29}$$

(Adrian 1984) and

$$F_I(\boldsymbol{s}) = \frac{1}{D_I^2} \int W'(\boldsymbol{x}) W''(\boldsymbol{x} + \boldsymbol{s})\, \mathrm{d}\boldsymbol{x} \tag{30}$$

(Adrian 1988), where D_I^2 is the area associated with the interrogation domain.

The terms R_C and R_F can be eliminated by subtracting the mean image intensity from I' and I''. The random correlation term $C'(\boldsymbol{s})$ reflects the fluctuation of a single realization with respect to the ensemble mean value.

Thus, the expected spatial correlation is essentially equal to the ensemble correlation, multiplied by a term that accounts for the in-plane loss of correlation (due to the tracer particles that enter and leave the interrogation domain). The amplitude of the correlation peak is proportional to $N_I F_I F_O$, where N_I is the so-called image density that reflects the mean number of particle images in an interrogation window.

3.2. Velocity gradients

The evaluation of images by a spatial cross-correlation implies that R_{GG} is evaluated over a finite measurement volume, i.e. $\delta V(\boldsymbol{X}') = \Delta Z_0 D_I^2$, which is depicted in figure 7.

Due to the spatial variations in the displacement over $\delta V(\boldsymbol{X}')$, the single displacement value that is represented by the δ-function in (24) is replaced by a displacement distribution function

$$R_D(\boldsymbol{s}) = N_I F_I F_O \cdot I_Z^2 t_0^2 F_t * \rho(\boldsymbol{s} - \boldsymbol{s}_D) \tag{31}$$

where $\boldsymbol{s}_D$ is a reference vector with regard to the 'position' of the displacement distribution. Hence, the displacement is no longer uniquely defined: $\boldsymbol{s}_D$ may now refer to the maximum of ρ (i.e. the most probable displacement) or the first moment of ρ (i.e. the local mean displacement) or, for that matter, any other convenient parameter that characterizes ρ.

The distribution has a finite width that is proportional to the local variation $|\Delta u|$ of the velocity. The total volume of the distribution remains constant, so when the distribution becomes broader, the peak amplitude decreases. Figure 8 shows the (one-dimensional) displacement distribution over a finite region for simple shear.

The broadening of the displacement-correlation peak has a negligible effect on R_D when the velocity differences over the integration volume are small with respect to the corresponding width of R_I, i.e.

$$|\Delta u| \Delta t \ll d_t / M \tag{32}$$

and the displacement field may be considered as locally uniform. In a practical situation d_t / D_I is about 3–5%; for larger gradients, the shape of the correlation peak may change significantly, and may even split up into several peaks. However, in the remainder of this paper it is assumed that equation (32) applies.

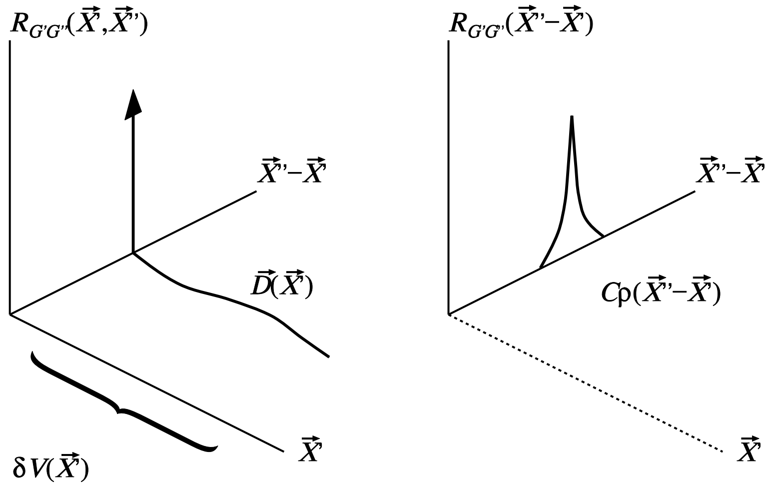

Figure 7. The integration of $R_{G'G''}$ over a small volume $\delta V(X')$ is replaced by a displacement distribution ϱ. (The horizontal axes actually represent three-dimensional spaces.)

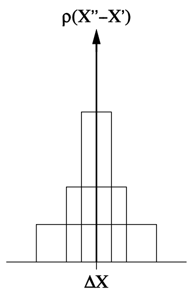

Figure 8. Velocity gradients broaden the displacement-correlation peak and reduce the peak amplitude.

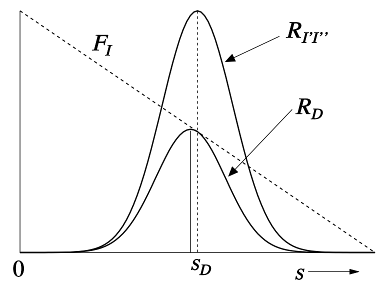

Figure 9. The displacement-correlation peak is skewed towards zero displacement as a result of the finite width of the peak and the finite size of the interrogation region.

3.3. Velocity bias

The result in equation (28) implies that the expectation of the spatial correlation estimate is equal to the true ensemble covariance peak multiplied by F_I. If W' and W'' are of equal size, then F_I always decreases as a function of the displacement magnitude. Consequently, the peak in R_D is slightly skewed towards the centre of the correlation domain, so that the maximum and first moment of the spatial correlation are biased towards smaller values (Adrian 1988) as shown in figure 9. The effect is proportional to the width of the correlation peak. This implies that the bias increases proportionally to the particle-image diameter. The bias is enhanced when there are significant velocity gradients over the interrogation window, as this further increases the width of the correlation peak.

In the literature this bias effect is often explained in terms of the number of particle–image pairs that can be contained within W. This is illustrated in figure 10. If there is a velocity gradient over W then the number of measurements from the smaller displacements is larger than that of the larger displacements, so the measured displacement is biased towards the smaller displacements. However, this does not explain the fact that the bias also occurs for uniform displacements, so the explanation of the bias in terms of particles is incorrect.

Figure 11 shows the difference between the measured and actual displacement for a uniformly displaced test image. The analysis was done with uniform and Gaussian window functions. The measurements yield a small bias which is constant for uniform W and proportional to the displacement for Gaussian W (Keane and Adrian 1990). Note that a bias occurs even when the displacement is uniform.

A typical value of the bias for a 32×32 pixel interrogation region is about 0.1 px (see figure 11). This can lead to significant errors in the estimation of the flow velocity statistics, or in the computation of derived flow quantities (e.g. vorticity), and it is therefore necessary to compensate for it.

The bias can be eliminated by dividing the spatial correlation by F_I (Westerweel 1993a, b); see figure 11. Another method that can be used to eliminate the bias is to use uniform interrogation windows with different sizes (Keane and Adrian 1993). In that case, part of F_I is constant (see figure 12) so that the displacement peak is not skewed.

Note that it does not make any difference with respect to the spatial correlation defined in (26) which of the windows is made larger, as is shown in figure 12. However, the common explanation is that W'' must be larger than W', so that all particles present in W' also appear in W''. This

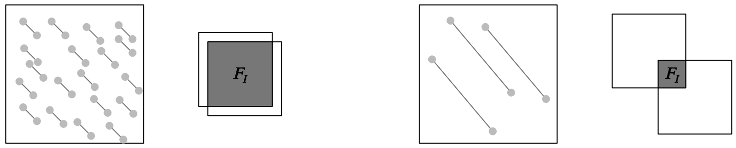

Figure 10. The number of particle–image pairs that can be contained in an interrogation region is reduced for increasing displacements.

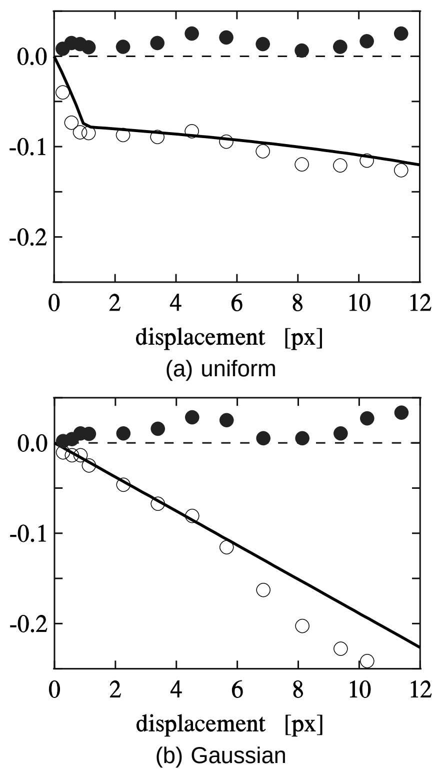

Figure 11. The difference between the measured and actual displacement as a function of the displacement for uniform and Gaussian window functions (○ without bias correction; ● with bias correction; —— theoretical bias value).

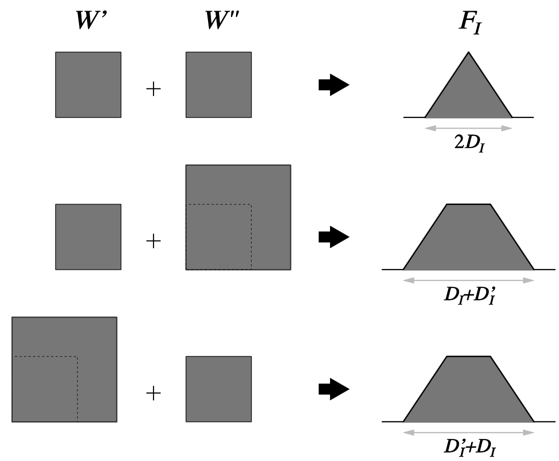

Figure 12. The effect of using differently sized interrogation windows.

intuitive explanation is incorrect as it implies that when W'' is *smaller* than W', the loss of particles is increased, which would enhance bias effects. However, when W' and W'' in (26) are interchanged (which essentially corresponds to a time reversal in the measurement) the outcome does not change. Again, an interpretation in terms of particles yields an incorrect description.

3.4. Implementation

To evaluate the spatial cross-correlation it is necessary that each image is recorded separately. It is not always possible or practical to do this, for example in high-speed applications. Therefore the two images are often superimposed in one recording, and the image is analysed with a spatial auto-correlation. In that case three dominant peaks appear (Adrian 1988): apart from the displacement-correlation peak (due to the correlation of I' with I''), a mirror peak appears (due to the correlation of I'' with I') on the opposite side of a central self-correlation peak (due to the correlation of I' with I', and I'' with I''); see figure 13(b). Since it is not possible to make a distinction between the two displacement-correlation peaks, there exists an 180° directional ambiguity for the direction of the displacement. Hence, the directional ambiguity should not be considered as a limitation of the method, but rather as a consequence of the particular choice for the implementation of the correlation estimator.

The Fourier transform of the spatial auto-correlation yields a fringe pattern where the fringe orientation is perpendicular to the direction of the displacement and the fringe spacing is inversely proportional to the magnitude of the displacement; see figure 13(c). The Fourier transformation can be implemented optically, which makes it possible to perform the analysis instantaneously. In the past this was a common implementation, but nowadays the images are digitized (either directly, or from photographic records) and processed numerically.

3.5. Optimization

Successful interrogation depends on the ability to identify the displacement-correlation peak R_D with respect to the random correlation C' (R_C and R_F are trivial terms). This implies that the amplitude of R_D has to be maximized, i.e. the term $N_I F_I F_O$. This has been investigated extensively by Keane and Adrian (1990, 1991, 1993) who specified 'design rules' for high image density PIV measurements:

$$N_I F_I F_O > 7 \quad \text{and} \quad M|\Delta u|\Delta t/D_I < d_t/D_I \approx 0.03\text{–}5. \tag{33}$$

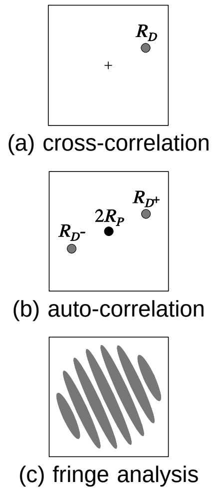

Figure 13. Different implementations for estimation of the displacement-correlation term.

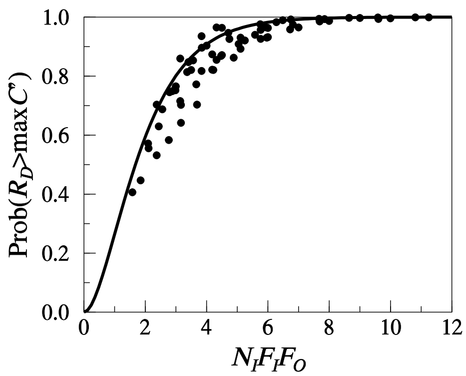

Figure 14. The probability that the displacement-correlation peak is larger than the random noise in the spatial cross-correlation. The symbols represent results from Monte Carlo simulation; the full curve corresponds to the probability that the interrogation window contains two or more particle images (after Keane and Adrian 1993).

For example, at an image density $N_I = 12$ the in-plane and out-of-plane displacements should be less than one-quarter of D_I and ΔZ_0 respectively (i.e. $F_I, F_O \geq 0.75$). To these rules should be added the requirement of using tracer particles that can be considered as ideal, and that are distributed homogeneously in the flow.

Figure 14 shows the probability that R_D is larger than the maximum of C' as a function of $N_I F_I F_O$ for 32×32 pixel cross-correlation with $d_t/d_r = 2$. The full curve represents the probability that the interrogation window contains at least two particle images.

4. Pixelization

This section discusses the aspects related to analysis of digital PIV images. Pixelization consists of sampling a signal in small image elements (pixels) and the subsequent quantization of the signal amplitude; see figure 15.

4.1. Bandwidth

An important aspect of digitization is the choice of the sampling rate that is required for the digital image to yield a 'correct' representation of the original continuous image. The sampling theorem (figure 16) states that a bandlimited signal can be reconstructed from its discrete samples without losses when the sampling rate of the signal is at least twice the signal bandwidth (Oppenheim *et al* 1983).

The optical system shown in figure 5 is bandlimited, with a bandwidth given by:

$$W = [(M+1) f^{\#} \lambda]^{-1} \tag{34}$$

(Goodman 1968), where λ is the light wavelength. For $f^{\#} = 8$, $M = 1$, and $\lambda = 0.5$ μm, the bandwidth is 125 mm^{-1}. This implies that a 1×1 mm^2 interrogation area should be sampled with a resolution of (at least) 256×256 pixels. This is a typical value used for the conventional analysis of PIV photographs.

In section 2.1 it was explained that variations in the displacement field scale with the magnitude of the displacement. Since the displacement is usually much larger than the particle-image diameter, the information with regard to the displacement field is contained in the low wavenumber range of the spectrum, whereas the high wavenumber range only contains information with regard to the detailed shape of the particle images. Hence, for the purpose of the measurement it is not necessary to resolve the full optical bandwidth.

An alternative definition of the signal bandwidth is the width of a cylinder which has the same total volume as the spectrum and the same height at zero wavenumber (see figure 17), i.e.

$$W_P = [\pi S(0,0)]^{-1/2} \tag{35}$$

which is referred to as the Parzen bandwidth (Oppenheim *et al* 1983). In this definition the detailed shape is ignored, and the bandwidth refers to a length scale that characterizes the length over which the correlation decays to zero. (Note that $S(0,0)$ is equal to the integral over the correlation peak, which is proportional to d_t^2.)

For the optical parameters given above the Parzen bandwidth is equal to 31 mm^{-1} (Westerweel 1993a, b), so that a resolution of 64×64 pixels for a 1×1 mm^2 area should be adequate. This value is typically used nowadays for PIV image interrogation (Prasad *et al* 1992).

4.2. Image sampling

The image $I(x, y)$ is commonly discretized with an electronic imaging device (usually a CCD) that 'integrates' the light intensity over a small area, referred to as a pixel. It is assumed that the device has a linear response with respect to light intensity and is made of square and contiguous pixels of area d_r^2. The discrete image $I[i, j]$ is then given by:

$$I[i, j] = \iint p(x - i d_r, y - j d_r) I(x, y)\, \mathrm{d}x\, \mathrm{d}y \tag{36}$$

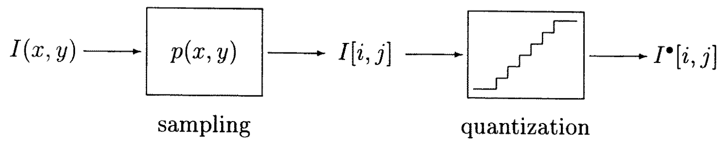

Figure 15. Pixelization of a continuous image consists of spatial sampling and the quantization of intensity values.

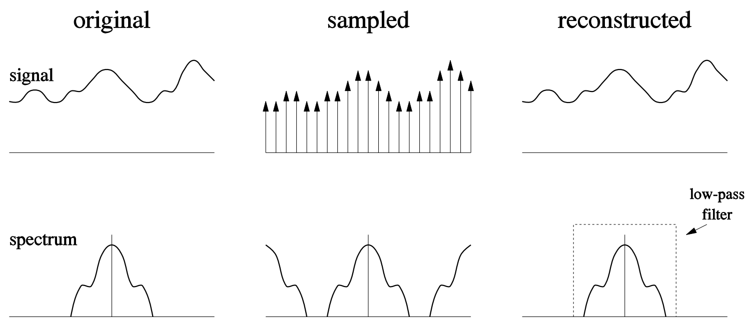

Figure 16. The sampling theorem.

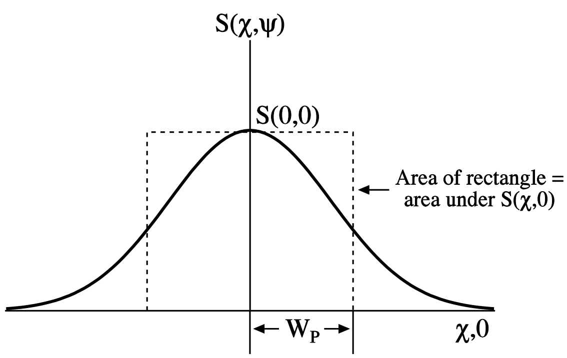

Figure 17. The signal bandwidth according to Parzen (after Oppenheim *et al* 1983).

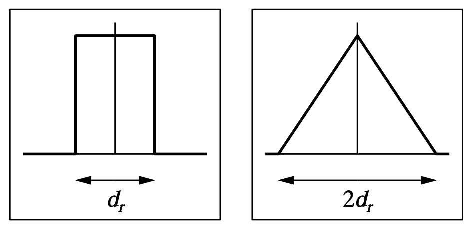

(a) $p(x, y)$ (b) $\Phi_{pp}(r, s)$

Figure 18. The spatial pixel sensitivity $p(x, y)$ and the corresponding self-correlation $\Phi_{pp}(r, s)$.

where $p(x, y)$ is the spatial sensitivity of the pixel, i.e.

$$p(x, y) = \begin{cases} 1/d_r^2 & |x|, |y| < d_r/2 \\ 0 & \text{elsewhere.} \end{cases} \tag{37}$$

The discrete cross-covariance of two images I' and I'' is defined as:

$$R[r, s] = \langle I'[i, j]I''[i+r, j+s]\rangle - \langle I'[i, j]\rangle\langle I''[i+r, j+s]\rangle \tag{38}$$

and substitution of (36) yields:

$$R[r, s] = \{\Phi_{pp} * R\}(rd_r, sd_r) \tag{39}$$

where Φ_{pp} is the self-correlation of the pixel sensitivity; see figure 18. Hence, the discrete correlation is given by the convolution of continuous correlation with Φ_{pp}, that is subsequently sampled at integer pixel values.

4.3. Quantization

The step subsequent to image sampling is quantization, by which the image intensity I is mapped onto a discrete variable $I^\bullet$ that takes values from a finite set of numbers. Descriptions of quantizer designs and their properties have been given by Jain (1989) and Rosenfeld and Kak (1982).

The relation between the quantizer input and output can be written as

$$I[m, n] = I^\bullet[m, n] + \zeta[m, n] \tag{40}$$

(see figure 19) where ζ denotes the quantizer noise. Provided that the number of levels is large with respect to the range of the input signal, ζ has (approximately) a uniform distribution, with the following statistical properties:

$$E\{\zeta\} = 0 \qquad E\{I^\bullet\zeta\} = 0 \qquad E\{I\zeta\} = E\{\zeta^2\} \tag{41}$$

(Jain 1989). Hence, the effect of quantization can be modelled as additive white noise. This will appear in the (cross-) correlation as a small δ-impulse at zero offset, i.e.

$$R^\bullet[u, v] = R[u, v] + E\{\zeta^2\} \cdot \delta[0, 0]. \tag{42}$$

Thus, for non-zero displacements the quantization error does not influence the evaluation of the correlation peak. This has been confirmed by Monte Carlo simulations (Willert 1996) which demonstrated that the random measurement error for the displacement is independent of the number of quantization levels.

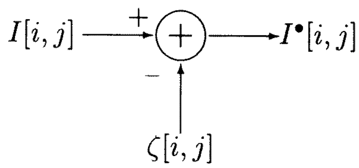

Figure 19. The quantization error can be considered as additive noise.

5. Digital analysis

5.1. Discrete spatial correlation

The spatial cross-covariance for two $N \times N$ pixel (interrogation) images I' and I'' is estimated with:

$$\hat{R}[r,s] = \frac{1}{N^2}\sum_{i=1}^{N}\sum_{j=1}^{N}(I'[i,j]-\bar{I})(I''[i+r,j+s]-\bar{I}) \quad (43)$$

where $\bar{I}$ is the (local) mean image intensity. The mean image intensity is subtracted to eliminate the terms R_C and R_F in (27). The expectation value for (43) is equal to

$$E\{\hat{R}[r,s]\} = F_I[r,s]\cdot R[r,s] \quad (44)$$

with

$$F_I[r,s] = \left(1-\frac{|r|}{N}\right)\left(1-\frac{|s|}{N}\right) \quad (45)$$

(cf equation (30)).

The spatial correlation of discrete images can be evaluated directly or by using discrete Fourier transforms (DFTs). It should be noted that the fast Fourier transform (FFT) is simply a fast and accurate algorithm (and not a method) to evaluate the double summation in (43).

One should be aware of the fact that the DFT applies to periodic signals. The correlation domain for (43) ranges from $-N+1$ to N for each component. Hence, the DFT should be carried out on a $2N \times 2N$ domain. This can be accomplished by padding I' and I'' with zeros. When the DFT is carried out over a smaller domain, then the part of the correlation that is not resolved is folded back onto the correlation. This is comparable to 'aliasing' in the frequency domain.

When the displacement complies with the PIV design rule in (33), i.e. $|s_D| < \frac{1}{4}D_I$, then the correlation is zero for $|r|, |s| > \frac{1}{4}N$. In that case, zero padding is not required, and the DFT can be carried out on an $N \times N$ domain. However, one should be cautious when evaluating multiple-exposure recordings. In that case, 'harmonic' correlation peaks appear at integer multiples of the position of R_D (Keane and Adrian 1991). The 'aliased' harmonic peaks can interfere with the evaluation of the R_D. This appears to cause a biasing effect for displacements equal to N/n, with $n = 1, 2, \ldots$ (Draad 1996). This is illustrated in figure 20.

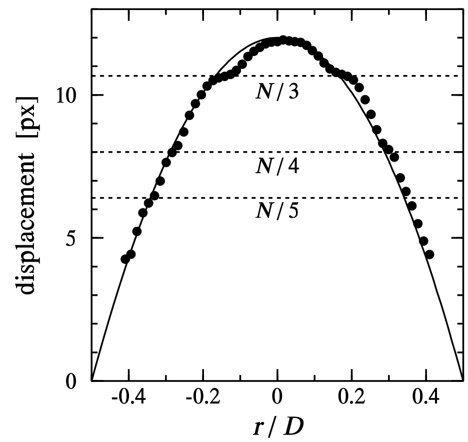

(a) *without* zero padding

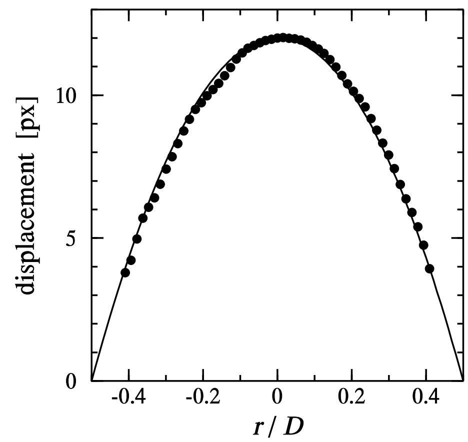

(b) *with* zero padding

Figure 20. Result of the evaluation of a multiple-exposure recording without and with zero padding, for the measured axial velocity in a laminar pipe flow. The measured displacement in pixel units is plotted as a function of the distance from the centreline divided by the pipe diameter (after Draad 1996).

5.2. Estimation of the correlation

The estimated correlation values are not independent 'samples' of the continuous image correlation but are correlated over a finite range. This can be expressed in terms of a correlation area L^2, i.e.

$$L^2 = \sum_t\sum_u \frac{\mathrm{cov}\{\hat{R}_D[r_D,s_D],\,\hat{R}_D[r_D+t,s_D+u]\}}{\mathrm{var}\{\hat{R}_D[r_D,s_D]\}} \quad (46)$$

where $[r_D, s_D]$ is the location of the displacement–correlation peak. The value of L^2 may be interpreted as the number of correlated samples, so that the ratio of N^2 to L^2 yields the effective number of 'independent' samples (Priestley 1992, Westerweel 1993a, b).

Figure 21 shows L as a function of d_t/d_r for the case of a 1×1 mm^2 interrogation region with $d_t = 25$ μm. For $d_t/d_r < 1$ the width of R_D is determined by Φ_{pp}, and L is $\mathcal{O}(1)$. For a narrow peak the correlation estimates are practically uncorrelated, which implies that an improvement of the resolution (i.e. the number of samples) increases the information content of the correlation peak.

For $d_t/d_r > 1$ the width of the correlation peak is proportional to d_t, and L is proportional to N. An improvement of the resolution does not mean that information is added; instead the same information is

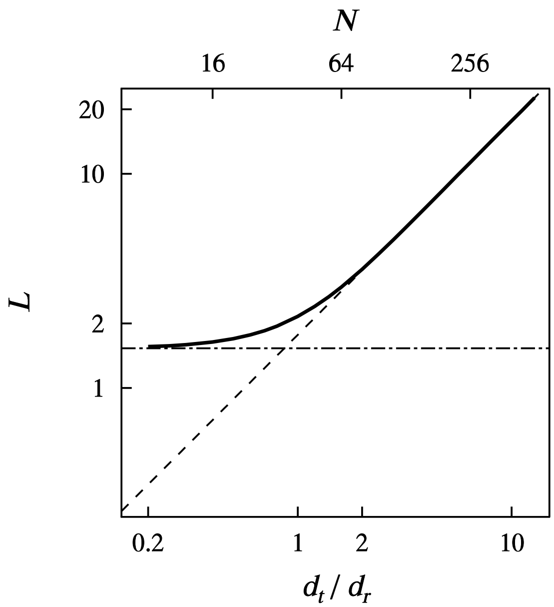

Figure 21. The effective number of uncorrelated samples in an interrogation window as a function of the pixel resolution for a 1×1 mm^2 interrogation area and 25 μm particle-image diameter.

simply distributed over more samples, and adjacent correlation values become more strongly correlated. Hence, the information content remains constant for increasing resolution. Note that the resolution for which L becomes proportional to N (i.e. $N > 64$) complies with the sampling rate based on the Parzen bandwidth.

The result in figure 21 indicates that the measurement resolution is determined by d_t/D_I and not by d_r/D_I, so that there is no difference in resolution and precision between results from photographic and digital PIV recordings as long as the value of d_t/D_I is equal. This has actually been verified by comparing photographic and digital PIV measurements in the same flow geometry under equivalent flow conditions (Westerweel *et al* 1996). The results demonstrated that there were practically no differences between photographic and digital PIV results, despite the fact that the resolution of the photographs was several orders of magnitude higher than that of the CCD camera. However, photographs can contain a larger (equivalent) number of pixels in comparison with CCD arrays, so that photographs can view a larger area of the flow; this aspect has been further explained by Adrian (1995).

5.3. Estimation of the fractional displacement

Consider the displacement-correlation peak at low pixel resolution, i.e. $d_t/d_r \sim 2$. If only the location of the maximum correlation were to be used, then the absolute measurement error would be $d_r/2$; for a 32×32 pixel interrogation area with a displacement of $(\frac{1}{4} \times 32 =)$ 8 px, this corresponds to a relative error of 6%. This not accurate enough for many applications.

When the correlation peak covers more than one pixel, the displacement can be determined at sub-pixel level by interpolation. This is even possible when the particle-image diameter is less than a pixel: note that the width of Φ_{pp} is $2d_r$ (for contiguous pixels), which implies that the discrete correlation peak always covers more than one 'pixel' in the correlation domain.

Figure 22 illustrates the appearance of the covariance for $d_t/d_r = 1.6$ at different fractional displacements. The strongest effect of the sub-pixel location is found in the correlation values adjacent to the maximum; these hold most of the information with respect to the fractional displacement. Only the direct neighbours of the maximum exceed the noise level (represented by the shaded area). Hence, for small d_t/d_r only *three* correlation values contain *significant* information with respect to the particle-image displacement in the associated direction. These three correlation values are subsequently denoted as R^*_{-1}, R^*_{+1} and R^*_{-1} respectively. Note that the unbiased correlation estimates are used (i.e. $R^* = \hat{R}/F_I$).

Two interpolation methods that are frequently used are the peak centroid and the Gaussian peak fit. The (sub-pixel) peak centroid is given by:

$$\hat{\epsilon}_C = \frac{R^*_{+1} - R^*_{-1}}{R^*_{-1} + R^*_0 + R^*_{+1})}. \tag{47}$$

The centroid estimator is based on the fact that the centroid of a symmetric object is equal to the position of the object (Alexander and Ng 1991). For the discrete correlation this is only true for $\epsilon = 0$ and $\frac{1}{2}$ (see figure 22). As a result, the centroid estimate for the fractional displacement is strongly biased towards integer values of the displacement in pixel units. This effect is known as 'peak locking', and is clearly visible in figure 23(a), which shows a histogram for the displacement measured in turbulent pipe flow (Westerweel *et al* 1996) using the peak centroid.

The Gaussian peak fit is based on the notion that the displacement-correlation peak has an approximately Gaussian shape:

$$\hat{\epsilon}_G = \frac{\ln R^*_{-1} - \ln R^*_{+1}}{2(\ln R^*_{-1} + \ln R^*_{+1} - 2\ln R^*_0)} \tag{48}$$

(Willert and Gharib 1991). As this estimator provides a better approximation of the actual peak shape, the peak locking effect is reduced considerably. For comparison, figure 23 also shows the displacement histogram obtained using equation (48).

Despite the differences in behaviour, the two estimators described above are quite similar: the numerator only contains R^*_{-1} and R^*_{+1}, while the denominator is a function of all three elements. This reflects the earlier observation that a fractional displacement most strongly affects R_{-1} and R_{+1}.

5.4. Estimation error

The variance of the estimated fractional displacement is approximated by

$$\mathrm{var}\{\hat{\epsilon}\} \approx \sum_{i=-1}^{+1} \sum_{j=-1}^{+1} \frac{\partial \hat{\epsilon}}{\partial R^*_i} \frac{\partial \hat{\epsilon}}{\partial R^*_j} \mathrm{cov}\{R^*_i, R^*_j\} \tag{49}$$

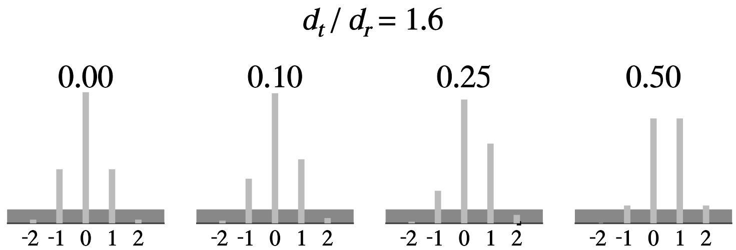

Figure 22. The correlation peaks for different values of the fractional displacement. The shaded area represents the 95% significance level of the background noise.

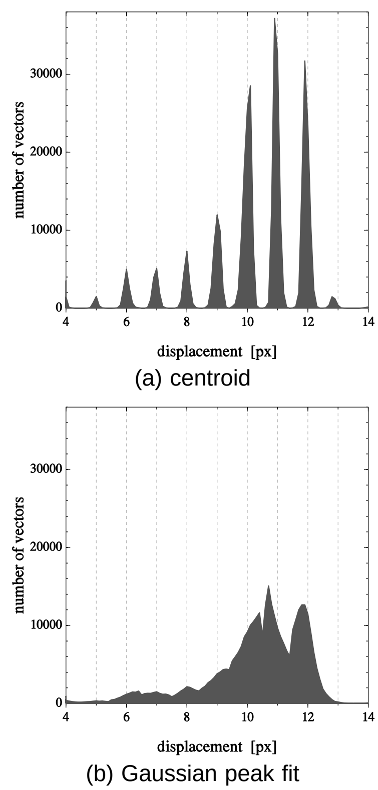

Figure 23. Histograms of the measured axial displacement in pixel in a turbulent pipe flow (Westerweel *et al* 1996), using the centroid and Gaussian peak fit for the sub-pixel interpolation.

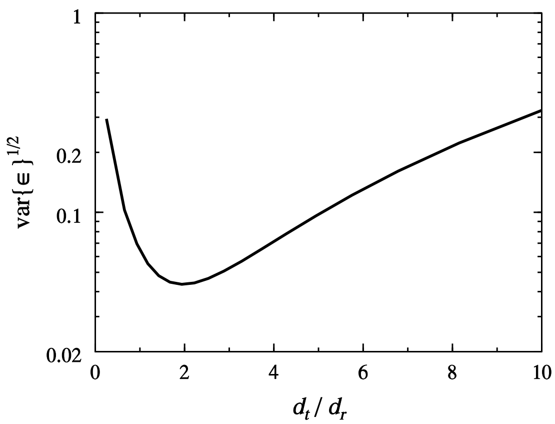

Figure 24. The rms estimation error for the fractional displacement as a function of particle image diameter in pixel units for a 1×1 mm^2 interrogation region with d_r = 31 μm (i.e. 32×32 pixel resolution).

(Westerweel 1993a, b) where $\partial\hat{\epsilon}/\partial R_i^*$ denotes the partial derivative of $\hat{\epsilon}$ with respect to R_i^*. Given that, for $\epsilon = 0$

$$\frac{\partial\hat{\epsilon}}{\partial R_0^*} = 0 \qquad \text{and} \qquad \frac{\partial\hat{\epsilon}}{\partial R_{-1}^*} = -\frac{\partial\hat{\epsilon}}{\partial R_{+1}^*} \tag{50}$$

the expression for $\mathrm{var}\{\hat{\epsilon}\}$ reduces to:

$$\mathrm{var}\{\hat{\epsilon}\} \approx \left(\frac{\partial\hat{\epsilon}}{\partial R_{\pm 1}^*}\right)^2 [\mathrm{var}\{R_{-1}^*\} + \mathrm{var}\{R_{+1}^*\} - 2\,\mathrm{cov}\{R_{-1}^*, R_{+1}^*\}]. \tag{51}$$

The first term only depends on the sub-pixel interpolation function, which reflects the observation that the precision is improved when the interpolation matches the shape of the correlation peak. The second term only depends on the statistical properties of the displacement-correlation peak. Note that this term would vanish if R_{-1}^* and R_{+1}^* were perfectly correlated. This only occurs for the case of a zero displacement (with zero quantization error; see (42)).

It was shown by Westerweel (1993a, b) that the first term is proportional to $1/R_D^2 = \mathcal{O}(N_I^{-2})$, whereas the second term is proportional to $R_D^2 = \mathcal{O}(N_I^2)$. This leads to the surprising conclusion that $\mathrm{var}\{\hat{\epsilon}\}$ does not depend on the image density, i.e. increasing the seeding density does *not* improve the estimation precision. This can also be observed in Monte Carlo simulation results (Willert 1996).

An explanation for this is that the correlation analysis is valid for (nearly) uniform displacements, so that all particle–image pairs have the same displacement; although the addition of particle–image pairs increases the amplitude of R_D, which enhances the detectability of the displacement-correlation peak, it does not add new information with regard to the displacement (i.e. all displacements are identical). So, the measurement *precision* is determined by d_t/D_I, whereas the measurement *reliability* is determined by N_I.

5.5. Optimal particle image diameter

Expression (51) is plotted in figure 24 for the Gaussian peak fit estimator as a function of d_t/d_r. This theoretical result complies with earlier empirical results by Prasad *et al* (1992), and simulation results obtained by Willert (1996). For $d_t/d_r \ll 1$ the measurement error is dominated by bias errors (i.e. peak locking), whereas for $d_t/d_r \gg 1$ random errors (that increase proportionally with the

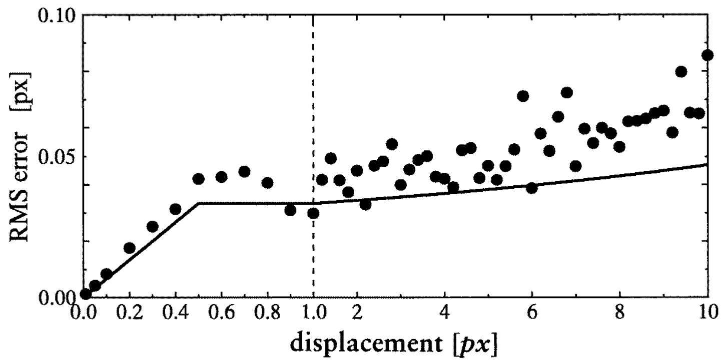

Figure 25. The random error amplitude as a function of the displacement for d_t/d_r=2 and D_I/d_r=32. The symbols are results of a Monte Carlo simulation; the full curve is the theoretical prediction according to (51) (after Westerweel *et al* 1997).

particle-image diameter) are dominant. The estimation error has a minimum at $d_t/d_r \sim 2$, with a value that is proportional to d_t/D_I (Willert 1996).

A typical value for the minimum measurement error is 0.05 to 0.1 pixel units for a 32 × 32 pixel interrogation region. This implies a relative measurement error of about 1% for a displacement that is one quarter of the interrogation window size.

5.6. Optimization of the estimation

The theoretical description of the statistical properties can be applied to optimize further estimations of the displacement. Figure 25 shows the theoretical prediction and simulation results for RMS measurement error ($\mathrm{var}\{\hat{\epsilon}\}^{1/2}$) as a function of the displacement for $W' = W''$. The error is almost constant over the complete range of displacements, except for very small displacements, where it decreases to zero. This change in behaviour is determined by the statistical properties of the estimated correlation: when the maximum displacement-correlation is located at $[0, 0]$ then $\mathrm{var}\{R^*_{-1}\} + \mathrm{var}\{R^*_{+1}\} \approx 2\,\mathrm{cov}\{R^*_{+1}, R^*_{+1}\}$; otherwise, $\mathrm{var}\{R^*_{-1}\} + \mathrm{var}\{R^*_{+1}\} > 2\,\mathrm{cov}\{R^*_{+1}, R^*_{+1}\}$.

When the interrogation windows are offset by the (integer part of the) particle-image displacement, the displacement-correlation peak is relocated near the origin. This does not only optimize the detectability of the displacement-correlation peak (Keane and Adrian 1993), but also reduces the measurement error. A further description is given by Westerweel *et al* (1997); the error reduction is demonstrated in measurements of grid turbulence and turbulent pipe flow.

However, a further improvement of the estimation precision does not automatically imply that the overall accuracy is improved by the same amount. For example, the measurement accuracy is also determined by the behaviour of the tracer particles, filtering effects due to the representation of the velocity field as a (locally uniform) displacement field, nonlinear effects of the imaging optics, etc., and at a certain point these effects become dominant. In that case it would be worthwhile to reduce D_I so that the estimation error (which is proportional to d_t/D_I) is at the same level as the other error sources. Hence, the window offset can be utilized to improve the *spatial* resolution of the measurement. An example is shown in figure 26, where a window offset was combined with a reduction in the size of the interrogation windows. At a spatial resolution of only 16 × 16 pixels with a 50% overlap between adjacent interrogations, 14 641 vectors were extracted from a single 1000 × 1016 pixel image.

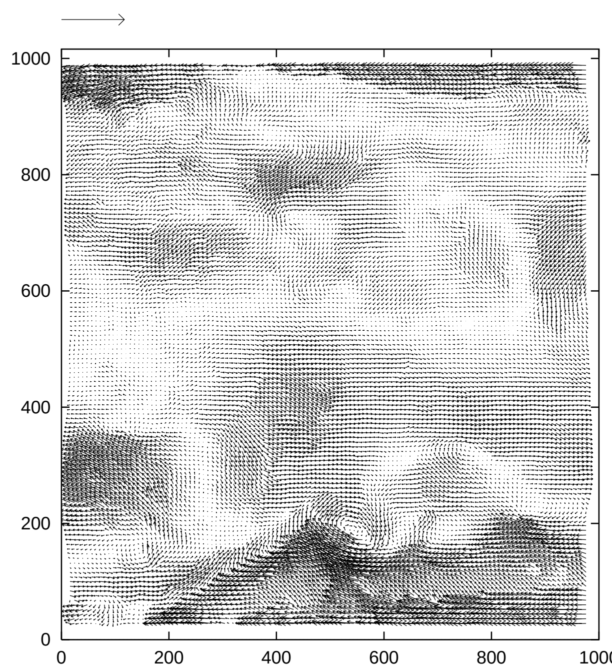

Figure 26. Velocity fluctuations relative to the mean velocity profile for a turbulent pipe flow (Westerweel *et al* 1996), obtained from a 1000 × 1016 pixel digital image that was interrogated with 16 × 16 pixel interrogation regions (with a window offset equal to the local particle-image displacement). The upper and lower axes coincide with the pipe wall; the large arrow at the top of the figure represents the mean particle-image displacement at the centreline (11.7 px).

6. Conclusion

The measurement principle has been generalized and is described in terms of linear system theory. The fluid motion is determined from a correlation of a tracer pattern that is tied to the fluid. The tracer pattern does not necessarily have to consist of discrete tracer particles. As a matter of fact, it was shown that an interpretation in terms of ‘particles’ does not always yield a consistent description of interrogation analysis. In principle it would also be possible for the tracer pattern to describe a continuous tracer, such as speckle or dye. It has been demonstrated that an interpretation of the image correlation in terms of the displacement is only valid for a statistically homogeneous tracer pattern.

The general picture that emerges from the description of the fundamental aspects of digital particle image velocimetry is that the limitations of the technique arise as direct consequences of particular implementation choices. For example, the representation of the velocity field as a displacement field implies a spatial and temporal low-pass filtering. Another example is the directional ambiguity that arises due to fact that the estimation of the image cross-covariance is implemented as a spatial auto-correlation. So, one may view the different ‘methods’ described in the literature as different ‘implementations’ of the same basic principle.

Further analysis of the signals showed that the measurement resolution is not determined by the pixel size, but by the particle-image diameter relative to the size of the interrogation region. The amount of information with regard to the particle-image displacement does not improve when the particle image has a diameter of more than two pixels; a further reduction of the pixel size corresponds to an over-sampling of the signal. Evidently, this applies to information with regard to the displacement (i.e. the location of the displacement-correlation peak) only; for other signal characteristics, such as peak amplitude (i.e. out-of-plane motion) and peak width (i.e. velocity gradients), the resolution requirements may be quite different.

The theory provides guidelines for optimization of the measurement technique. An explanation of why the number of quantization levels is not significant with respect to the measurement precision has been given. It has also been shown that the measurement reliability is determined by the image density, whereas the measurement precision is determined by the particle-image diameter.

Finally, the theory is also useful to further improve the performance of the method. The noise reduction effect for interrogation analysis with a window offset could be used to improve the spatial resolution. Further improvements may be expected by optimizing the sub-pixel interpolation with respect to the shape of the discrete displacement-correlation peak.

Acknowledgment

The research of dr ir J Westerweel has been made possible by a fellowship of the Royal Netherlands Academy of Arts and Sciences.

References

Alexander B F and Ng K C 1991 *Opt. Eng.* **30** 1320
Adrian R J 1984 *Appl. Opt.* **23** 1690
——1988 Statistical properties of particle image velocimetry measurements in turbulent flow *Laser Anemometry in Fluid Mechanics* ed R J Adrian *et al* (Lisbon: Instituto Superior Tecnico) pp 115–29
——1991 *Ann. Rev. Fluid Mech.* **22** 261
——1995 Limiting resolution of particle image velocimetry for turbulent flow *Advances in Turbulence Research* pp 1–19
Draad A A 1996 *PhD Thesis* Delft University of Technology
Goodman J W 1968 *Introduction to Fourier Optics* (New York: McGraw-Hill)
Jain A K 1989 *Fundamentals of Digital Image Processing* (Englewood Cliffs, NJ: Prentice-Hall)
Keane R D and Adrian R J 1990 *Meas. Sci. Technol.* **1** 1202
——1991 *Meas. Sci. Technol.* **2** 963
——1993 *Appl. Sci. Res.* **49** 191
Keane R D, Adrian R J and Zhang Y 1995 *Meas. Sci. Technol.* **6** 754
Oppenheim A V, Willsky A S and Young I T 1983 *Signals and Systems* (Englewood Cliffs, NJ: Prentice-Hall)
Prasad A K, Adrian R J, Landreth C C and Offutt P W 1992 *Exp. Fluids* **13** 105
Priestley M B 1992 *Spectral Analysis and Time Series* 7th edn (San Diego, CA: Academic)
Raffel M, Westerweel J, Willert C, Gharib M and Kompenhans J 1996 *Opt. Eng.* **35** 2067
Rosenfeld A and Kak A C 1982 *Digital Picture Processing* 2nd edn (Orlando, FL: Academic)
Westerweel J 1993a *Digital Particle Image Velocimetry — Theory and Application* (Delft: Delft University Press)
——1993b Optical diagnostics in fluid and thermal flow *SPIE* **2005** 624–35
Westerweel J, Dabiri D and Gharib M 1997 *Exp. Fluids* **23** 20
Westerweel J, Draad A A, van der Hoeven, J G Th and van Oord J 1996 *Exp. Fluids* **20** 165
Willert C E 1996 *Appl. Sci. Res.* **56** 79
Willert C E and Gharib M 1991 *Exp. Fluids* **10** 181